Double Pendulum

M. Clark[a], J. Blumoff[a], S. Rah[a], J. Robinson[a]

[a] *Georgia Institute of Technology*

Abstract

The double pendulum is a classic dynamical system, capable of chaotic behavior in a four-dimensional phase space. The driven case introduces even more peculiar behaviors and opens the possibility for stable folded modes. In this paper, we explore the double pendulum in both driven and undriven cases through experimental observation and simulations, focusing on time-to-flip as a major measure of chaotic behavior.

1. Introduction and theory

A double pendulum consists of two simple pendula, with the second arm attached to the end of the first. Both arms must be capable of a full range of motion in the plane of interest. A valid way to achieve this is to have the upper (first) arm be hollow, so that the second arm may swing through it. Regardless of the exact model, however, a simple diagram of the system is in Figure 1 [1].

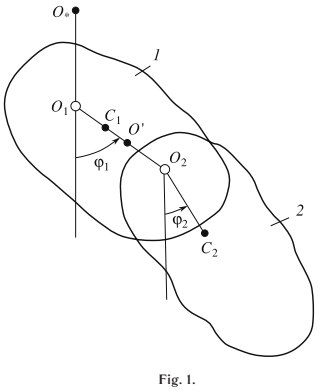

Fig. 1.

Figure 1: Kholostova fig. 1: model of the general double pendulum.

For the discussion to follow, let l deonte the distance from the first arm's center of mass to the point where the second arm is mounted to it. Let b_1 and

b_2 denote distances between respective arms' centers of mass to their mounting points (for the first arm, the entire system's point of suspension; for the second arm, the point of attachment to the first). φ_1 and φ_2 represent angles compared to hanging vertically downward, with corresponding angular velocities $\dot{\varphi}_1 = \omega_1$ and $\dot{\varphi}_2 = \omega_2$. The arms have densities ρ_1 and ρ_2 and thus masses m_1 and m_2. In the driven case, if the driving force on the suspension point is sinusoidal, we have

$$O_* O_1 = a \sin(\Omega t) \tag{1}$$

where Ω is the oscillation frequency. The theory of double pendulum (and the more general driven case) is expounded upon by Kholostova in much more detail. His final result, however is thus:

$$\dot{\varphi}_1 = \frac{\rho_2^2 - \hat{p}_{\varphi_1} - l b_2 \cos(\varphi_1 - \varphi_2)\hat{p}_{\varphi_2}}{m_1 \rho_1^2 \rho_2^2 + m_2 l^2 [\rho_2^2 - b_2^2 \cos^2(\varphi_1 - \varphi_2)]} \tag{2}$$

$$\dot{\varphi}_2 = \frac{m_1 \rho_1^2 + m_2 l^2)\hat{p}_{\varphi_2} - m_2 l b_2 \cos(\varphi_1 - \varphi_2)\hat{p}_{\varphi_1}}{m_2(m_1 \rho_1^2 \rho_2^2 + m_2 l^2 [\rho_2^2 - b_2^2 \cos^2(\varphi_1 - \varphi_2)])} \tag{3}$$

Where the momenta $\hat{p}_{\varphi_1}$ and $\hat{p}_{\varphi_2}$ are given by

$$\begin{aligned} \hat{p}_{\varphi_1} = {} & (m_1 \rho_1^2 + m_2 l^2)\dot{\varphi}_1 + m_2 l b_2 \dot{\varphi}_2 \cos(\varphi_1 - \varphi_2) \\ & - (m_1 b_1 + m_2 l) a \Omega \sin \varphi_1 \cos \Omega t \end{aligned} \tag{4}$$

$$\begin{aligned} \hat{p}_{\varphi_2} = {} & m_2 \rho_2^2 \dot{\varphi}_2 + m_2 l b_2 \dot{\varphi}_1 \cos(\varphi_1 - \varphi_2) \\ & - m_2 b_2 a \Omega \sin \varphi_2 \cos \Omega t \end{aligned} \tag{5}$$

with the potential energy of the arms given by

$$H = -(m_1 b_1 + m_2 l) g \cos(\varphi_1) - m_2 b_2 g \cos(\varphi_2) \tag{6}$$

We forward-integrate these equations of motion to achieve numerical verification of our experimental trials.

2. Numerical modeling

To verify our experimental data, we consider the energetic requirements for the second arm to flip fully—to invert itself compared to the vertical. There must be a minimum energy requirement in the system, below which we can tacticly predict that no configuration is capable of flipping.

$$E_{\min} = [(m_1 b_1) + m_2(1 - b_2)]\, g \tag{7}$$

This equation is valid when the initial conditions have no angular momentum, as we strove to achieve in our experiment. Using this simple energetic consideration allowed us to quickly verify and dismiss all initial conditions below this thredhold, but again, while it is a necessary condition to be capable of

flipping, it is not a sufficient one. Anecdotally, we observed several states that, despite having enough energy from a gravitational standpoint, quickly settled into modes as described in [2], even when their amplitudes weren't small-angle. Thus, this is only a very rough way to reduce the set of initial conditions for a numerical exercise.

By symmetry, we could eliminate half of the angular phase space for one of the angle parameters. Clearly, vertical symmetry makes the initial condition $(\varphi_1, \varphi_2) \equiv (-\varphi_1, -\varphi_2)$. Restricting φ_1 to positive values is a simple way to take advantage of this symmetry and reduce the size of the simulation space.

Since time-to-flip has no simple analytic solution, we considered both simulation schemes and numerical integration. Our first attempt drew upon WorkingModel2D to simulate the system, but the inability to run these sims faster than real-time proved a significant hindrance, even at cutting off simulations beyond 10 seconds. This procedure also had issues of extracting data for processing from the program, ultimately leading to loss of resolution. To improve upon this model, we chose to forward-integrate Equation 4 and Equation 5 in MATLAB.

3. Experiment

The rig for our experiment consisted of two aluminum arms, each roughly 30 cm in length and of 0.2 kg in mass. Both arms had full, 360-degree range of motion, with the second arm able to rotate freely while "passing" through the first. To alter the parameters of the experiment, we used attachable lead weights, each individually about 1 kg in mass, to change the relative masses of the arms. For driving experiments, the rig was mounted atop an electromagnetically-driven speaker. This system was capable of up to 6 Hz oscillations with maximum amplitude of 5 cm.

3.1. Data collection methods

3.1.1. Accelerometry

Our initial prospect for collecting data from the double pendulum system rested on an Analog Devices ADXL321 accelerometer, rated to $\pm 18g$. Using a single accelerometer, we hoped to collect enough information from the system to reconstruct the angles of each arm and their associated angular velocities. A diagram of the accelerometer reference frame is in Figure 2.

The use of this single accelerometer is insufficient, however, to fully characterize the system. A proof of this is as follows.

For convenience, it will be easier if, instead of considering how this reference frame translates compared to the lab frame, we consider another reference frame with the same origin as the lab frame (that is, the x and y-axes would then be simply rotated compared to the lab frame).

Again, for convenience, let $w = u + iv = b_1 \exp i\varphi_1 + b_2 \exp i\varphi_2$. Geometrically, then, $x+iy = w \exp i(\pi - \varphi_2)$. This neatly defines how to achieve a change

of coordinates, and we can now convert lab accelerations to the accelerometer reference frame. Let $x + iy = z$. Then

$$z = b_1 e^{i(\pi+\varphi_1-\varphi_2)} - b_2 \tag{8}$$

$$\dot{z} = ib_1 e^{i(\pi+\varphi_1-\varphi_2)}(\dot{\varphi}_1 - \dot{\varphi}_2) \tag{9}$$

$$\ddot{z} = b_1 e^{i(\pi+\varphi_1-\varphi_2)} \left[(\dot{\varphi}_1 - \dot{\varphi}_2)^2 + i(\ddot{\varphi}_1 - \ddot{\varphi}_2)\right] \tag{10}$$

The accelerometer gives information about proper accelerations along the two axes, x and y. This proper acceleration also has a component of magnitude g directed upwards compared to real acceleration as measured in the lab frame (that is, the accelerometer measures acceleration with a free-fall geodesic as a zero baseline). Thus, the u-component of proper acceleration is $a_u = \ddot{u} - g$. Since this is rotated compared to the accelerometer's axes, the measured (proper) acceleration is

$$\ddot{z}_{\text{proper}} = b_1 e^{i(\pi+\varphi_1-\varphi_2)} \left[(\dot{\varphi}_1 - \dot{\varphi}_2)^2 + i(\ddot{\varphi}_1 - \ddot{\varphi}_2)\right] - g e^{i(\pi-\varphi_2)} \tag{11}$$

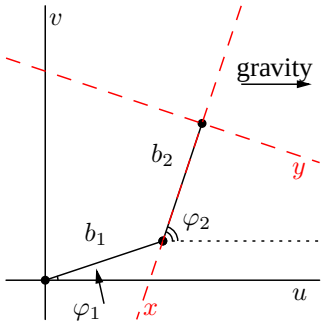

Figure 2: The rotated reference frame of an accelerometer mounted near the end of the second arm. u and v represent directions in the laboratory frame, with positive u being vertical down. The accelerometer, being fixed mounted to the second arm, defines a moving, rotating reference frame, whose axes are the red dashed lines, x and y. The origin of the lab frame is the suspension point of the first arm.

Measuring the x and y-components of this quantity and extracting the relevant angles proved, ultimately, too unappealing compared to simpler and more attractive alternatives that would determine these angles directly. In addition, while the accelerometer had a stated data acquisition rate of up to 600 Hz for the two combined channels, we found the data to be extremely noisy, even after post-process filtering.

Figure 3: The final rig setup, with black tracking strip in place on the second arm of the pendulum. The first arm is taped white to reduce shadows and tracking artifacts.

3.1.2. High-speed camera methods

Rather than heavily process accelerometer data, we opted to to use a high speed camera, capable of up to 100 frames per second, to optically resolve the positions of the two arms. Using National Instruments' Labview software, we were able to track individual dots affixed to the pendulum arms with ease, but the particular design of the rig posed problems for tracking. Labview could track in real time a dot (or several dots) using individually-sized search boxes, but occlusion of these tracking dots by support struts confused the program, ultimately causing it to lose track of its assigned dots.

At the cost of real-time tracking, we instead taped a black tracking strip to the second arm, which provided robustness against partial occlusions (the horizontal support, however, could still occlude the whole arm in certain configurations). For later processing, we saved footage of each run of the system in raw bitmap files. To improve detection, we adjusted the contrast on the camera, such that it would detect only the most extreme black and white. This allowed us to ignore all but our own interference when we reset the pendulum for a run at a new set of initial conditions.

Processing of this footage to determine angles and momenta is described below. An image of the final rig is in Figure 3.

3.2. Procedure

For our experimental data collection, we sampled the phase space of the undriven and driven double pendulum for various initial conditions, always as close to zero angular momentum (for both arms) as possible. Without more safeguards and mechanisms to ensure these conditions, we could only approximate this, although for at least the undriven case, extraneous movements could

be detected and purged from the footage or the data point outright invalidated. For the undriven case, which produced our best data, we took 100 data points at varying initial conditions, hoping to probe the region between flip-capable and flip-incabable states.

3.3. Data processing

Significant post-processing was required to arrive at usable data from the experimental trials. We start with the undriven case as the principal basis for processing techniques, followed by modifications for the driven case.

3.3.1. Undriven case

We converted the raw footage (with resolution 320 by 240 in 8-bit grayscale) to binary pixel data—pixels with darkness less than 150 out of 255 were set to white (no detection). Everything darker than this was assumed to be part of our detection strip on the second arm. To process the data further, the observed detection strip was eroded, dilated, and thinned. A final morphing process detected the endpoints of the strip, necessary to more easily determine the position of the first arm (which had no such strip). We performed a linear regression on all the "dark" points in the image to calculate the slope (and thus, the angle) of the second arm. We also calculated the centroid of the second arm by averaging the coordinates of all the pixels within the strip.

To detect a flip, the centroid is a convenient measure, for when the cendroid crosses the circle defined by the joint between the first and second arms, it's possible a flip has occurred—at the least, this is a necessary condition, though not a sufficient one. Other related conditions are that the slope changes sign but with a high magnitude (that is, not around zero). In short, for there to be a flip,

$$\operatorname{sgn}(m_{i-1}) \neq \operatorname{sgn}(m_i) \tag{12}$$

$$|m_{i-1}| > 1, \quad |m_i| > 1 \tag{13}$$

$$|\vec{r}_s - \vec{r}_c|^2 < \ell_1^2 \tag{14}$$

where m_n refers to the slope at frame n, $\vec{r}_s$ is the position of the suspension joint between the arms, and $\vec{r}_c$ is position of the centroid of the second arm. ℓ_1 is the length of the first arm. To baseline these measurements (pixels versus centimeters), we held a meterstick to the first arm with the aperture at normal contrast.

While it might be possible to automatically extract the first frame i such that these flip conditions are satisfied in any given data video, in practice the first frames (even several seconds) of a data point must be carefully examined for flips performed before the release of the pendulum.

It should be noted that there is some ambiguity about the angle φ_2 for any given slope m; after all, for a given angle θ, $\theta - \pi$ also produces the same slope. To attack this problem, we found the intercepts of the regression line on the

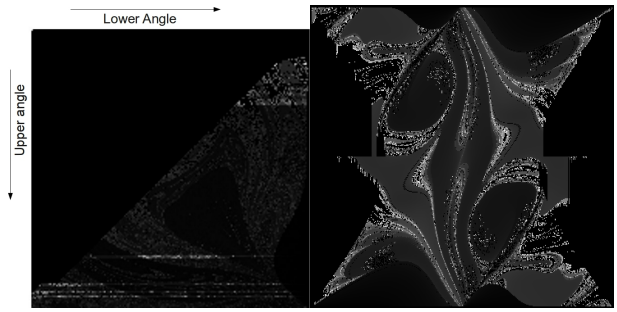

(a) Basic fractal, angles range from $-\pi$ to π

(b) Fractal recentered about $\varphi_1 = \pi$

Figure 4: Time to flip (dark: no flip; lighter: faster flip) on two-dimensional phase space

circle traced out by the upper-lower arm joint. Except for flips, the intercept closest to an endpoint is the joint. When the arm flips, we check against recent angles and choose the angle that results in the least change in angle. This can, then, result in a calculated joint position that is further from the arm endpoint.

3.3.2. Driven case

To aid in tracking the driven case, we attached a tracking point to the point of suspension and excluded this point from all footage except to verify the amplitude and frequency of the driven oscillation.

4. Results

Based on the numerical methods, we observed that the pattern of initial conditions in (φ_1, φ_2) space that produce a flip (and, moreover, the time it takes for any given initial condition to produce a flip) forms an interesting fractal pattern, one that is indicative of the fundamental attractor that governs this system.

To check these results against our experimental data, we plotted our undriven experiment data on top of the numerically-based fractal. In large part, the data are in good agreement, although the border cases would be improved with better resolution of the initial conditions.

Overall, we feel that with a more systematic means to choose and setup initial conditions, with a driving amplitude that is more capable of probing the stability of the inverted states, this double pendulum system would be quite suitable to illustrate a rich chaotic system.

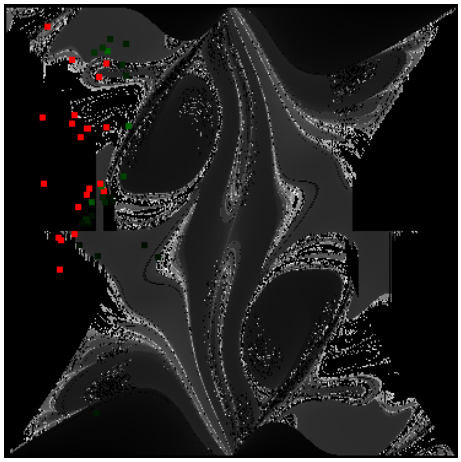

Figure 5: Underiven double pendulum data overlaid in red (no flip) and shades of green (lighter for shorter flip time) on top of the WorkingModel simulation fractal

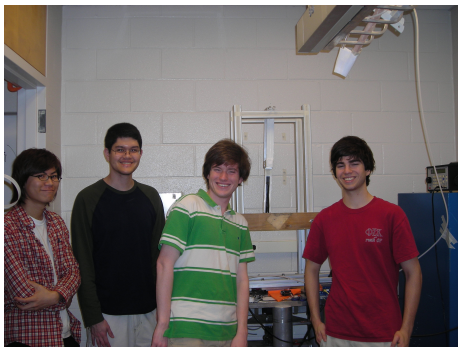

Figure 6: The double pendulum team

References

[1] O. V. Kholostova, On the motions of a douple pendulum with vibrating suspension point, Mechanics of Solids 44 (2) (2006) 25–40.

[2] R. B. Levien, S. M. Tan, Double pendulum: an experiment in chaos, American Journal of Physics 61 (6) (1993) 1038–1044.